Segmented medical images based simulations of Cardiac electrical activity and electrocardiogram: a model comparison

Charles Pierre, Olivier Rousseau, Yves Bourgault

SEGMENTED MEDICAL IMAGES BASED SIMULATIONS OF CARDIAC ELECTRICAL ACTIVITY AND ELECTROCARDIOGRAM: A MODEL COMPARISON.

by

Charles Pierre, Olivier Rousseau & Yves Bourgault

Abstract. — The purposes of this work is to compare the action potential and electrocardiogram computed with the monodomain and bidomain models, using a patient-based two-dimensional geometry of the heart-torso. The pipeline from CT scans to image segmentation with an in-house level set method, then to mesh generation is detailed in the article. Our segmentation technique is based on a new iterative Chan-Vese method. The bidomain model and its approximation called the "adapted" monodomain model are next introduced. The numerical methods used to solve these two models are briefly presented. Using both uni- and two-dimensional test cases, we next assess the mesh size required to control the error on the conduction velocities, a main source of error in cardiac action potential computations. We show with quantitative estimates that a main parameter controlling the mesh size is the cell membrane surface-to-volume ratio, noted χ. Realistic χ of about $1500 - 2000$ cm^{-1} for human hearts still require major computational resources. We then compare our numerical solutions and the electrocardiogram recovered with both models on our heart-torso geometry. Activation sites are chosen so that the depolarisation isochrons closely match experimental results in human hearts for healthy cardiac propagation. Both models give similar solutions whereas the bidomain model is about 20-50 times more CPU intensive than the adapted monodomain model. The main computational effort goes in the computation of the extra-cellular and extra-cardiac potentials in the heart-torso. We show that the equations for these potentials must be solved with sufficient accuracy, otherwise compromising the quality of the computed electrocardiograms.

Key words and phrases. — Electro-cardiology, bidomain and monodomain models, image segmentation, ECG simulation, reaction diffusion equations, numerical simulations.

1. Introduction

The numerical simulation of biological phenomenon requires to have both well suited/accurate models and precise data on the biological structures considered. Since models in electrocardiology are formulated in terms of partial differential equations, being able to generate precise meshes of the heart and of the surrounding tissue is a major asset towards a realistic simulation of the heart electrical activity. The general objective of this paper is to provide a complete pipeline *"Medical image analysis-Modelling-Simulation"* and to present the benefits of this synergetic strategy in comparing two models (namely the *bidomain* and the *adapted monodomain* models) for the computation of electrocardiogram (ECG) on a patient-based geometry built from CT scan medical data. Our simulations will concentrate on the normal cardiac electrical activity.

During every heartbeat, the so called *cardiac action potential* phenomenon occurs: the myocardium is successively crossed by two transmembrane potential waves – a depolarisation wave followed by a repolarisation one – respectively causing its contraction and relaxation. Cardiac action potential is due to ionic transfers across the cellular membrane inducing rises and drops in the intra- and extra-cellular potentials, the difference of which is the previously mentioned transmembrane potential. This activity generates an extra-cardiac potential field that varies over time and space, the measurement of which on the body surface is the ECG.

Cardiac electrical activity involves different complexity levels. Firstly at the cellular level, huge advances have been done from the pioneering works of Hodgkin and Huxley [**27**] to model ionic transfer across the cell membrane. Recent models provide an accurate description of mammalian myocites electrophysiology [**35**], human designed models of ventricle cells now being available [**47**].

Secondly, at a macroscopic tissue level, excitation process in myocardial tissue is the subject of numerous experimental studies, among which we non extensively quote *e.g.* [**10, 46, 45**]. Excitation process involves two quantities: the extra-cellular and the transmembrane potentials. The bidomain model [**49**] expresses the relationship between these two quantities as being linked by a current conservation balance law. Early simulation using the bidomain model have been done in [**42**].

Finally, at the body scale, the interaction between the heart and the surrounding tissues has been experimentally studied in [**36**] using perfused

dog hearts embedded in an electrolytic bath representing the torso. This study suggests a strong coupling between the extra-cellular and extra-cardiac potential fields.

The bidomain model has the strong advantage to be based on a clear and physiologically relevant modelling process including an homogenisation step from a microscopic tissue scale to a macroscopic one. This step has been formally derived in [**29**] and mathematically justified in [**2, 20**]. This underlying interpretation at a microscopic tissue scale makes possible the embedding of the bidomain model with a full torso model *via* physiologically relevant coupling conditions at the heart/torso interface [**30**], allowing the simulation of the extra-cardiac potential field and of the ECG. For these reasons the bidomain model is very popular for the simulation of the heart and torso coupled electrical activity [**32, 33**].

Meanwhile, the bidomain model is numerically highly demanding and various simplifications of this model have been widely used. The eikonal model [**15, 16, 12, 14**] allows to model the spread of transmembrane potential wavefront during depolarisation. Automaton models [**34**] allows the simulation of repolarisation sequence assuming the cells to have a *black box* behaviour determined by a single entry depolarisation signal only. Extra-cardiac potential fields can also be recovered during the depolarisation sequence using the oblique dipole layer representation [**18, 17, 13**]. All these simplified version of the bidomain model have their own limitations: simulation of a depolarisation sequence only, recovery of the extra-cardiac potential fields under strong limitations on the extra-cardiac domain geometry and structure for instance. Moreover, the simulation of body surface potential using these models follows a two steps strategy: first interpret the transmembrane potential wavefront as a distribution of current sources (dipoles), then calculate the associated far-field potential. As it has been pointed out in [**6**] and numerically validated in [**7**], this strategy does not properly capture the feedback between the extra-cellular and extra-cardiac potential fields above mentioned.

Another simplified variant of the bidomain model, referred to as the *monodomain model*, expresses the excitation sequence with the help of a single potential variable: the transmembrane potential only. This decoupling between the extra-cellular and the transmembrane potential fields is based on a non-physiologically relevant assumption referred to as the *equal anisotropy ratio assumption*. However, complex patterns of excitation in a realistic framework have been successfully simulated using the

monodomain model [**4, 43, 38**]. Although efficient in practise, the question of the coupling between the cardiac region where no extra-cellular potential is available and the extra-cardiac potential in the torso remained pending within the monodomain framework.

More recently, [**9, 19, 41**], a new model referred to as the *adapted monodomain model* was proposed both to address the bidomain model high computational cost problem and the coupling difficulty between the cardiac and extra-cardiac regions for the monodomain model. In this framework, the transmembrane potential field is governed by a single reaction diffusion equation as for the monodomain model, the computation of which remains decoupled from the extra-cellular/-cardiac potential fields. A complete extra-cardiac/-cellular potential field is then reconstructed from the transmembrane potential which construction naturally includes the physiological coupling between extra-cardiac and extra-cellular potentials on the heart surface. The adapted monodomain model has to be considered as an approximation of the bidomain model, providing both a much lower computational cost (since the extra-cardiac/-cellular potential field can be computed when desired only) and a correct coupling on the heart surface between the extra-cardiac and extra-cellular potential fields. The bidomain and adapted monodomain models have been compared in few papers. In [**9, 19**], the transmembrane potential course predicted by each model has been compared on a slab of tissue, respectively in dimension 2 and 3. A deep investigation on the excitation patterns and action potential duration is provided in [**19**], showing that the two models do match quite closely. In [**41**], extra-cellular potentials recordings on the epi- and endo-cardial surface have been simulated on an isolated three dimensional heart. Again the two models provided results in good agreement.

In this paper we propose to deepen the comparison between the bidomain and monodomain adapted models on ECG computations as well as transmembrane and extra-cellular/extra-cardiac potential fields on a realistic test case. Precisely, a two dimensional test case is considered, the geometry of which has been automatically generated from a patient based medical CT scan, which also includes both conductivity anisotropy inside the myocardium (due to the muscular fibre orientation) and conductivity heterogeneity inside the torso (where three different regions have been identified, namely the lungs, the ventricle cavities and the remaining tissues).

Patient-based geometry and meshes are generated from raw medical images using segmentation techniques that are presented in section 2. The bidomain and adapted monodomain models are stated and discussed in section 3, whereas section 4 is devoted to their practical implementation. Section 5 assesses the numerical difficulties of the two models, especially the mesh size requirements that have been evaluated on a simple two dimensional geometry. Last section 6 presents our realistic test case built from the segmented medical images. The simulations of both models on this test case are presented and eventually discussed. A concluding section follows.

2. Imaging and geometry

To run the numerical simulations in section 6, a mesh accurately reproducing the heart geometry and the torso organs boundaries is needed. This is done in two steps. First, we segment the heart and the torso from a medical image, next, we generate a mesh based on this segmentation. The image analysis tools developed in order to build this mesh are presented here.

Figure 1(a) represents a high resolution CT scan, courtesy of the Ottawa Heart Institute. The CT scan has size $512 \times 512 \times 199$ pixels. The horizontal resolution is of 0.49×0.49 mm whereas vertically it is of 1.25 mm. The heart geometry considered in section 6 has been extracted from the image shown on Figure 1(b). This image is a horizontal slice of the original three-dimensional CT scan exhibiting a cut through the two cardiac ventricles as well as a fraction of the lungs.

The medical image can be thought as a function $g : \Omega \to \mathbb{R}$. The segmentation is then performed using the Chan-Vese method [**8**], which seeks for an approximation of the image g with a binary (two colours) image $u : \Omega \mapsto \{c_1, c_2\}$. An energy functional is associated to this binary image, which energy will be minimised.
The minimisation space is denoted by X, it is defined as the set of all functions reading $u = c_1\chi_F + c_2\chi_{\Omega-F}$, where:

- χ_F is the indicator function of $F \subset \Omega$,
- $F \subset \Omega$ is a sub domain of sufficient regularity (with finite perimeter, see *e.g.* [**1**]),
- c_1, $c_2 \in \mathbb{R}$ are scalar constants.

(a) 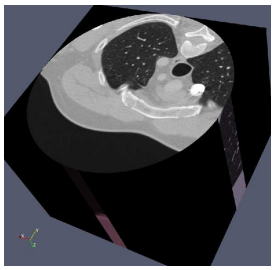 (b) 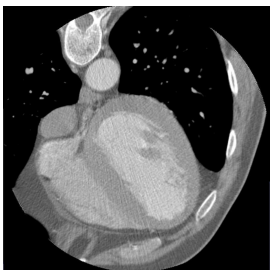

FIGURE 1. Medical images. (a) Three-dimensional CT scan (courtesy of the Heart Institute, University of Ottawa), with resolution 0.49×0.49×1.25 mm: 52 166 656 voxels. (b) Two-dimensional slice of the previous image, including an horizontal cut through the cardiac ventricles surrounded by the lungs.

We search for a solution u minimising the Mumford-Shah energy functional E_{MS} [**1, 37**] over X:

$$\min_{u\in X} E_{MS}(u) = \min_{u\in X} |J(u)| + \int_\Omega |g-u|^2\,dx\ , \tag{1}$$

where $|J(u)|$ denotes the perimeter of F for $u = c_1\chi_F + c_2\chi_{\Omega-F}$ (*i.e.* the $d-1$-dimensional Hausdorff measure of the jump set of u).
Problem (1) is reformulated using level sets. The unknown u is written using a level set function ϕ: $u = c_1 H(\phi) + c_2(1-H(\phi))$, where H denotes the Heaviside function. The energy functional in (1) can be reformulated in the level set framework and the associated Euler-Lagrange equations can be derived [**8**]. These equations are solved using a gradient descent method. A level set function ϕ associated to a solution of (1) thus is sought as a steady state of the following equations (δ standing for the Dirac measure):

$$\begin{aligned} \frac{\partial\phi}{\partial t} &= \delta(\phi)\left(\mu\ \mathrm{div}(\frac{\nabla\phi}{|\nabla\phi|}) + \lambda((g-c_2)^2 - (g-c_1)^2)\right) \\ c_1 &= \frac{\int_\Omega gH(\phi)}{\int_\Omega H(\phi)} \qquad c_2 = \frac{\int_\Omega g(1-H(\phi))}{\int_\Omega (1-H(\phi))}. \end{aligned} \tag{2}$$

System (2) has been numerically solved using an explicit finite difference scheme on the underlying image grid.

The Chan-Vese method provides a two-phase approximation of the image g, in other words the image is split in two sub-regions F and

$\Omega - F$. In order to segment images containing more than two phases, the method is applied once. Among the two phases so obtained, the one containing more than one region of interest is selected and considered as a new domain on which the Chan-Vese method is applied again. This iterative segmentation process is used until all the regions of interest within the original image g are fully extracted. This process is similar to the hierarchical segmentation method proposed by Tsai, Yezzi and Willsky [**48**].

Figure 2 shows the results of this process on the two-dimensional image of the heart depicted on Figure 1(b). The first step of the process provides the lungs geometry, which organs were the most contrasted part of the original image. The second step provides the epicardium and the last step the endocardium.

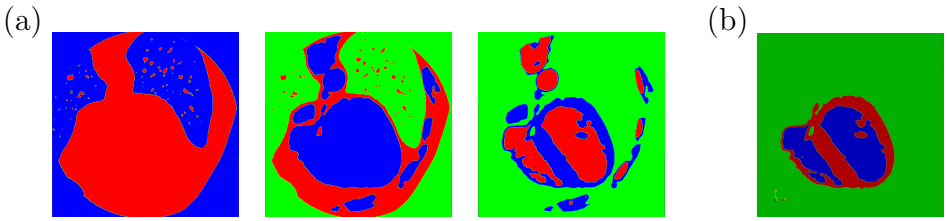

FIGURE 2. Segmentation process. (a) Iterative segmentation of the CT scan slice. From left to right: lungs boundary, epicardial and endocardial identifications. (b) Final image of the ventricle slice.

The final segmented image of the ventricle slice depicted on Figure 2(b) is then used to build a mesh of the cut through the torso, heart and lungs. The mesh generation has been performed using the code *DistMesh* [**39**], a mesher well suited for domains implicitly defined with level set functions. The mesh of the whole horizontal torso slice so generated is depicted on Figure 2. Four sub-domains have been identified on this mesh corresponding to 4 sub-meshes (cardiac region, ventricle cavities, lungs and remaining tissues). The boundary edges of these sub-meshes fit the segmented image sub-domains. Each sub-mesh has its own space resolution as related to the further simulation demands: the elements within the cardiac ventricles being much finer than the elements in the extra-cardiac domain.

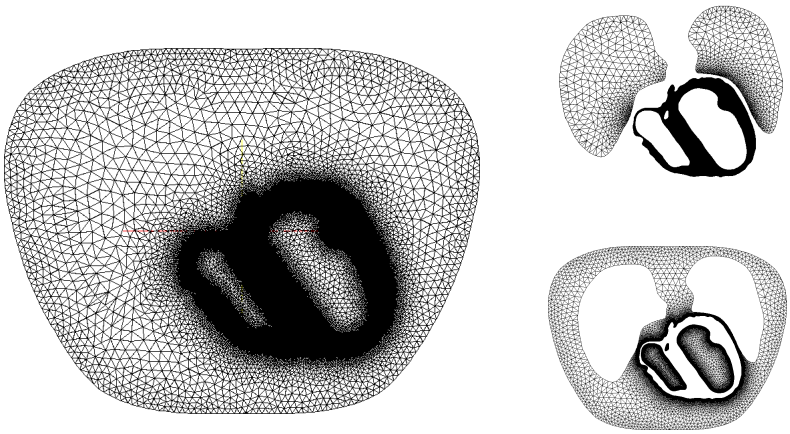

FIGURE 3. Mesh generation. Left: whole mesh. Top right: the lungs and the cardiac ventricles sub-meshes. Down right: the ventricular cavities and the surrounding tissues.

3. Electrocardiology model: mathematical formulation

The entire domain (the thorax slice) is denoted by Ω. The cardiac sub-domain is denoted H. For convenience, the extra-cardiac sub-domain is referred to as the *torso* and denoted $T = \Omega - \overline{H}$.
Two models are formulated in this section. Firstly the *bidomain* model for the heart embedded in the torso. Secondly a simplified version of this model, referred to as the *adapted monodomain* model.

3.1. Bidomain model for the heart embedded in the torso. —

3.1.1. Heart model. — At the microscopic scale (see *e.g.* [**20, 50**]) the cardiac tissue is regarded as being composed of two distinct media, the intra-cellular *(i)* and extra-cellular *(e)* media. These media interact across the active cellular membrane. This interaction is described by ionic models discussed in section 3.3.
The bidomain model provides an homogenised version of such microscopic model at the heart level [**2, 29**]. It involves two potential fields: the *intra-* and *extra-cellular potentials* ϕ_i and ϕ_e, respectively, in the whole cardiac volume H. The *transmembrane potential* V is defined as:

$$V = \phi_i - \phi_e \quad \text{in} \quad H. \tag{3}$$

At the macroscopic level, the cardiac tissue is seen as an arrangement of cardiac fibres rotating around the ventricle cavities (see fig. 8 below), thus

being tangent to the cardiac boundaries (endo- and epi-cardial). This fibre distribution determines the tissue anisotropy: at any point $x \in H$ is associated two conductivity tensors $\sigma_i(x)$ and $\sigma_e(x)$ corresponding to the intra- and extra-cellular media conductivity properties. These tensors are symmetric positive definite. Introducing the conductivities $g_{i,e}^l$, $g_{i,e}^t$ longitudinal and transverse to the fibres, these tensors read:

$$\sigma_i(x) = \mathrm{Diag}(g_i^l, g_i^t) \ , \quad \sigma_e(x) = \mathrm{Diag}(g_e^l, g_e^t) \ , \tag{4}$$

in an orthonormal base whose principal direction is given by the fibre orientation at point x.
The first equation of the bidomain model expresses, in absence of external current sources, the global current conservation between the intra-cellular and extra-cellular media. It reads:

$$\mathrm{div}(\sigma_i \nabla \phi_i) + \mathrm{div}(\sigma_e \nabla \phi_e) = 0 \quad \text{in} \quad H \ . \tag{5}$$

The second equation of the bidomain model comes from the cellular membrane modelling. The current between the intra- and extra-cellular media across the membrane is the sum of an ionic transfer (resistive current) and a capacitive current. At the macroscopic level, it reads:

$$\chi \left(c \partial_t V \ + \ I_{ion}(V, \mathbf{w}) \right) = -\mathrm{div}(\sigma_e \nabla \phi_e) \ , \tag{6}$$

c denoting the membrane surface capacitance, I_{ion} the surface current distribution on the membrane. χ is a homogenisation term defined as the rate of cellular membrane surface per unit volume. Not to enter the details of electrophysiology modelling, one shall simply present $\mathbf{w}(x,t) \in \mathbb{R}^N$ as a vector describing the state of the cellular membrane. Ionic models describing I_{ion} read the generic form:

$$\partial_t \mathbf{w} \ = \ g(V, \mathbf{w}) \quad \text{in} \quad H \ , \tag{7}$$

more precisions being given in section 3.3.

3.1.2. Torso model. — The torso T is considered as a passive conductor. Introducing the extra-cardiac potential field ϕ_T, one has:

$$\mathrm{div}(\sigma_T \nabla \phi_T) \ = \ 0 \quad \text{in} \quad T \ , \tag{8}$$

where σ_T is the conductivity tensor in T. This tensor is isotropic but heterogeneous, $\sigma_T(x) = g(x) Id$, assuming different conductivities g_L, g_C and g_R in the lungs, the ventricle cavities and the remaining tissues,

respectively. No current leaking out from the body, one has the following zero flux boundary condition:

$$\sigma_T \nabla \phi_T \cdot \mathbf{n} \;=\; 0 \quad \text{on} \quad \partial\Omega \;. \tag{9}$$

Eventually, heart and torso models are coupled on the heart surface by interface continuity conditions between the extra-cellular and extra-cardiac potentials [**30**]:

$$\phi_e = \phi_T \quad \text{and} \quad \sigma_T \nabla \phi_T \cdot \mathbf{n} = \sigma_e \nabla \phi_e \cdot \mathbf{n} \quad \text{on} \quad \partial H \;, \tag{10}$$

together with a zero flux condition on ϕ_i:

$$\sigma_i \nabla \phi_i \cdot \mathbf{n} = 0 \quad \text{on} \quad \partial H \;. \tag{11}$$

Conditions (10) (11) have the following interpretation at the microscopic level: the intra-cellular media is not in contact with the torso tissues and no current flows out of the intra-cellular media towards the extra-cardiac media. Therefore, all the interaction between the heart and the torso relies on the extra-cellular media.

3.2. Adapted monodomain model. — In the bidomain model framework, the transmembrane potential V on one hand and the extra-cellular/extra-cardiac potentials ϕ_e, ϕ_T on the other hand appear as being strongly coupled. Precisely, substituting $\phi_i = V + \phi_e$ in equation (5), one gets the elliptic PDE:

$$\mathrm{div}((\sigma_i + \sigma_e)\nabla \phi_e) \;=\; -\mathrm{div}(\sigma_i \nabla V) \;.$$

Together with (8) (9) (10), this can be seen as an equation defining $\phi_e(t)$ and $\phi_T(t)$ at time t as a function of $V(t)$. Meanwhile, incrementing (6) in order to get $V(t + \delta t)$ requires to know $\mathrm{div}(\sigma_e \nabla \phi_e)$ and thus ϕ_e. This process expresses the nature of the coupling between V and ϕ_e / ϕ_T and implies that one of these two quantities cannot be computed separately from the other.

This strong coupling raises several problems:

- From the numerical point of view, this coupling introduces an elliptic equation that has to be solved at each time step, thus meaning the inversion of one large ill-conditioned linear system per time step.
- From the physiological point of view, a strong coupling between ϕ_e and ϕ_T has been evaluated and confirmed in [**36**], meaning that one of this two fields cannot be derived independently from the other. During normal activation of the heart, no strong coupling linking V to ϕ_e, ϕ_T has been clearly identified in physiological studies. This

has been evaluated in [**36**] using measurements on a perfused human heart. Thus, V appears as being independent from ϕ_e, ϕ_T. Therefore only a weak coupling,– where ϕ_e, ϕ_T are functions of V and where V is independent from ϕ_e, ϕ_T–, is relevant in terms of model for a normal activation sequence of the heart.

In [**5**], it has been showed in a simplified framework involving an isolated heart, that the bidomain model can be reformulated as follows:

$$\chi\,(c\partial_t V \;+\; I_{ion}(V,\mathbf{w})) = \mathcal{A}V \;, \quad \partial_t \mathbf{w} = g(V,\mathbf{w}) \;. \tag{12}$$

In this equation, $\mathcal{A}$ denotes a pseudo-differential operator, precisely being defined as the harmonic mean of the two elliptic operators $\mathrm{div}(\sigma_i\nabla\cdot)$ and $\mathrm{div}(\sigma_e\nabla\cdot)$. This operator is *non-differential* in general: its definition requires an elliptic problem inversion which procedure is *non local*. The strong coupling between V and ϕ_e, ϕ_T precisely relies on the non differential nature of the operator $\mathcal{A}$.
However, although $\mathcal{A}$ is non-differential in general, it turns out to become differential in very particular (non generic) cases. In the case of *equal anisotropy ratio* it is assumed that there exists a constant c such that $\sigma_e(x) = c\;\sigma_i(x)$ in H). In this case one gets:

$$\mathcal{A} = \mathrm{div}(\sigma_m\nabla\cdot) \;, \quad \text{where} \quad \sigma_m := (\sigma_i^{-1} + \sigma_e^{-1})^{-1}. \tag{13}$$

σ_m appears to be the harmonic mean of σ_e and σ_i. This particular case is known as the *monodomain model*. In the framework of the monodomain model, equation (6) is a relation between V and $\mathbf{w}$ only, and V then decouples from ϕ_e, ϕ_T. Therefore, V can be computed independently, implying a considerable speed up in the computations since no elliptic system inversion is required to increment V.
The equal anisotropy ratio assumption however is non-physiologically relevant, and the monodomain model can not be handled under this form.

3.2.1. Adapted monodomain model statement. — The *adapted monodomain model* is an approximation of the bidomain model where the strong coupling between V and ϕ_e, ϕ_T discussed above is weakened. Precisely, the operator $\mathcal{A}$ in (12) is here replaced by the following differential operator:

$$\mathcal{A} \;\simeq\; \mathrm{div}(\sigma_m\nabla\,\cdot\,) \;, \quad \sigma_m = (\sigma_i^{-1} + \sigma_e^{-1})^{-1} \;. \tag{14}$$

This approximation is exact in the case of equal anisotropy ratio. The computations resulting from the adapted monodomain model proceeds as:

1. First step. Compute the membrane potential V using the reaction diffusion model in H only,

$$\chi\left(c\partial_t V + I_{ion}(V,\mathbf{w})\right) = \mathrm{div}(\sigma_m \nabla V)\ , \quad \partial_t \mathbf{w} = g(V,\mathbf{w})\ , \tag{15}$$

   using the following zero flux boundary condition on V,

$$\sigma_m \nabla V \cdot \mathbf{n} \ = \ 0 \quad \text{on } \partial H\ . \tag{16}$$

   This condition is discussed in Remark 1.
2. Second step. Using the precomputed value of $V(t)$ at time t, compute the extra-cardiac and extra-cellular potentials $\phi_T(t)$, $\phi_e(t)$ by solving in Ω the elliptic problem (5), (8) with (9)-(10). This could be done *when wanted only and not at each time step.*

Remark 1. — *The zero flux condition* (16) *has no physiological foundation. It however provides a convenient and correct approximation of the situation within the bidomain framework. First of all let us again point out that due to the tangency of the muscular fibre on the heart boundary, this condition actually reads* $\nabla V \cdot \mathbf{n} = 0 = \nabla\phi_i \cdot \mathbf{n} - \nabla\phi_e \cdot \mathbf{n} = -\nabla\phi_e \cdot \mathbf{n}$ *on* ∂H *using* (11). *Since* $\nabla\phi_e \cdot \mathbf{n} \neq 0$ *in general, condition* (16) *does not strictly hold with the bidomain model. However, because the variation on the potential* V *is limited except in the sharp de-/re-polarisation wavefronts,* $\nabla V \cdot \mathbf{n}$ *appears as being negligible on* ∂H *excepted in the small region where the wavefront is in contact with* ∂H*, so a posteriori justifying* (16). *More detailed numerical illustrations on this point are given in section 6.2.*

3.3. Models settings. —

3.3.1. Ionic models. — From the pioneering work of Hodgkin and Huxley [**27**], a considerable amount of work has been devoted to obtain accurate and realistic descriptions of cellular membrane electrical activity. In the past decade, great improvements have been made towards the modelling of mammals ventricular cells electrophysiology, especially since Luo and Rudy class II models [**35**], allowing the modelling of calcium behaviour and of several electrophysiological disturbances such as ischemia. A human designed version of this model, the TNNP model [**47**], will be

Model parameters	**Values**	**Unit**
Cell membrane surface-to-volume ratio	$\chi = 1500 - 2000$	$[\text{cm}^{-1}]$
Membrane surface capacitance	$c = 1.$	$[\mu\ \text{F/cm}^2]$
Longitudinal intra-cellular conductivity	$g_i^l = 1.741$	[mS/cm]
Transverse intra-cellular conductivity	$g_i^t = 0.1934$	[mS/cm]
Longitudinal extra-cellular conductivity	$g_e^l = 3.906$	[mS/cm]
Transverse extra-cellular conductivity	$g_e^t = 1.970$	[mS/cm]
Lung conductivity	$g_L = 0.5$	[mS/cm]
Blood conductivity (ventricle cavities)	$g_C = 6.7$	[mS/cm]
Remaining tissues conductivity	$g_R = 2.2$	[mS/cm]

TABLE 1. Parameters calibration.

used to model ionic currents in all our simulations. An action potential predicted by this model is depicted on figure 4.

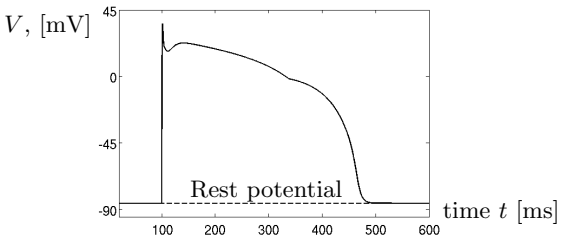

FIGURE 4. Trans-membrane potential predicted by the TNNP ionic current model for human ventricular cells [**47**].

3.3.2. Parameters. — Both the cardiac conductivity parameters and the homogenisation factor χ determines the depolarisation wavefront velocity. Physiological measurements of this velocity along and across the cardiac fibres can be found in Clerc's paper [**10**] or in a series of paper by Spach *et al.* [**45, 46**]. Spach *et al.* pointed out strong individual variability as well as age influence both on propagation velocities and longitudinal/axial velocities ratio. In this paper, we use the conductivities from [**31**], which parameters have been computed in order for the model predictions to fit the experimental measurements. These values are given in table 1. They imply an axial/transverse velocity ratio of 2.6. Setting the cell membrane surface-to-volume ratio χ to 1800, the model axial and transverse velocities are of 0.5 and 0.19 m/s, respectively. All these values are in good agreement with the ranges in [**45**]. The value of χ also has a strong individual and age variability, a range of 1500-2000

cm^{-1} seems suitable. The setting of this parameter in regard to numerical difficulties is detailed in section 5. The conductivity values for the different torso component have been found in [**44**].

4. Model numerical implementation

Discrete unknowns. For both the bidomain and the adapted monodomain models, two unknowns are computed at every time step n on the heart mesh: the transmembrane potential V^n and the gating variable associated with the ionic model $\mathbf{w}^n$. Note that V^n is a one column vector whereas $\mathbf{w}^n$ is a N columns vector depending on the chosen ionic model. For the model considered here, N is of order 20.

Let us introduce the discrete potential field $\phi^n = \begin{cases} \phi_e^n & \text{in } H \text{ mesh} \\ \phi_T^n & \text{in } T \text{ mesh} \end{cases}$, defined on Ω's mesh thanks to the continuity condition (10).

For the bidomain model, ϕ^n has to be computed at each time step.

For the adapted monodomain model, ϕ^n is computed when desired only, here at each millisecond.

Time discretisation. A semi-implicit Euler scheme is used here: implicit for the diffusion and explicit for reaction terms. Although more precise time integration schemes have been pointed out in [**25**], attention is focused here on the space discretisation.

Space discretisation For the 1D simulations in section 5.1, a finite differences method has been used.

For all the remaining simulations in dimension 2, more sophisticated numerical methods on triangular meshes are needed to numerically solve the bidomain and the adapted monodomain models. A finite volumes method has been used here, referred to as *DDFV* method (Discrete Duality Finite Volumes [**23, 26**]).

Finite volumes schemes have been showed in [**21**] to exhibit good stability properties with regard to the sharpness of the reaction terms. Moreover, *DDFV* schemes have been especially designed for solving anisotropic/heterogeneous diffusion problems [**22**]. They provide an accurate description both of the scalar potential field and of the vector current field, which seems to be well appropriated here. Adaptation of this method to electrocardiology problems has been presented in [**40**].

One essential property of this scheme is to preserve the symmetry and positivity properties of the diffusion operators at the discrete

level, so allowing a wide range of linear solvers and preconditioning techniques. Precisely, denoting by σ some general tensor (anisotropic, heterogeneous), one has the following discretisation of the diffusion equation:

$$\text{div}\,(\sigma \nabla u) \;=\; f \quad \stackrel{\text{disc.}}{\longrightarrow} \quad A_\sigma U \;=\; D\; F\;, \tag{17}$$

where A_σ is a symmetric non positive matrix and D is a diagonal positive matrix.

Bidomain model implementation. At each time step, the following two operations are performed:

1. Solve the linear system

$$\begin{bmatrix} D & \dfrac{\Delta t}{\chi c}\, A_{\sigma_e} \\ \tilde{A}_{\sigma_i} & A_{\overline{\sigma}} \end{bmatrix} \begin{bmatrix} V^{n+1} \\ \phi^{n+1} \end{bmatrix} \;=\; \begin{bmatrix} D\left(V^n - \dfrac{\Delta t}{c} I_{ion}(V^n, \mathbf{w}^n)\right) \\ 0 \end{bmatrix}\;,$$

   with the notations in (17) and where:
   - $\overline{\sigma}$ is the tensor $\sigma_i + \sigma_e$ in H and σ_T in T,
   - $\tilde{A}_{\sigma_i} V^{n+1}$ is equal to $A_{\sigma_i} V^{n+1}$ in H and to 0 in T.

   Each line of the system corresponds to the discretisation of equations (6) and (5)+(8), respectively, and where the constraints (9)-(10) are directly imposed within the construction of the three matrices A_{σ_i}, A_{σ_e} $A_{\overline{\sigma}}$.

   The resulting linear system has a non-symmetric global matrix composed of symmetric blocks. A GMRES solver with SSOR preconditioning has been used.
2. Update the gating variables $\mathbf{w}^{n+1}$ by solving the ionic model *ODE* system (7).

Adapted monodomain model implementation. It follows the same procedure as for the bidomain model but the first step is greatly simplified.

1. Invert the linear system (on H only):

$$\left(D \;-\; \frac{\Delta t}{\chi c}\, A_{\sigma_m}\right) V^{n+1} \;=\; D\left(V^n - \frac{\Delta t}{c} I_{ion}(V^n, \mathbf{w}^n)\right)\;.$$

   This system has a symmetric positive-definite global matrix. A CG solver with a SSOR preconditioning is used.
2. Update the gating variables $\mathbf{w}^{n+1}$ by solving the ionic model *ODE* system (7).

The potential ϕ is recovered at each millisecond only by inverting the balance equations (5)+(8) on Ω. At the discrete level, it reads:

$$A_{\overline{\sigma}}\phi^k = -\tilde{A}_{\sigma_i}V^k \ ,$$

with the same notation as previously. This system has a symmetric negative definite matrix and can be solved using a CG solver with SSOR preconditioning.

Updating the gating variables $\mathbf{w}^n$. At each time step, the reaction differential system (7) is solved point-wise using classical ODE solvers, either forward Euler or better with Runge-Kutta 4 (RK4) for stiff equations (to resolve fast inward sodium currents). Numerical simulations showed that such a solver provides an approximation of high accuracy since the time step required by this RK4 method is of the order of 1 ms, which value is much larger than the time steps of less than 0.1 ms used in further computations with the coupled ODE/PDE system.

5. Assessing mesh size requirements

When simulating the propagation of transmembrane potential waves, an accurate prediction of both the wavefront velocity and the action potential duration (ADP) is of primary importance.
APD is defined pointwise as the time interval between depolarisation and repolarisation. This quantity is controlled by the differential system (7), therefore no great influence of the space discretisation on the APD has been observed in numerical simulations.
On the hand, the wavefront velocity is highly sensitive to the space discretisation, which dependence was expected since transmembrane potential wave propagation is due to diffusion processes in the wavefront region. Thus, an accurate description of the transmembrane potential within the wavefront region is necessary, which requires a fine enough space resolution. Since the wavefront thickness and velocity are proportional to $1/\chi$, a relationship between the space resolution requirements and the scaling parameter χ is crucial.

The purpose of this section is precisely to investigate numerically what space resolution is required in order to obtain an accurate description of the wavefront. First of all, one-dimensional experiments are presented to exhibit the general behaviour of the discrete solutions. Secondly, this behaviour is confirmed with a more complex 2D framework to determine

quantitative space resolution requirements as depicted in table 2. These 1D and 2D results are discussed together.

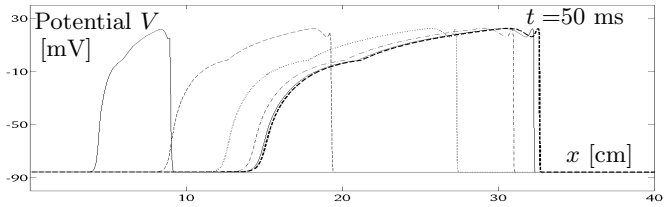

FIGURE 5. Transmembrane potential waves (pulses) propagation along a 40 cm muscular fibre for different mesh resolution Δx. Pulses are recorded at time $t = 50$ ms. From left to right, the pulses correspond to a resolution of 1, 0.5, 0.25, 0.125 and 0.06125 mm respectively. The bold dash line (reference solution) correspond to a $\Delta x = 0.0075$ mm.

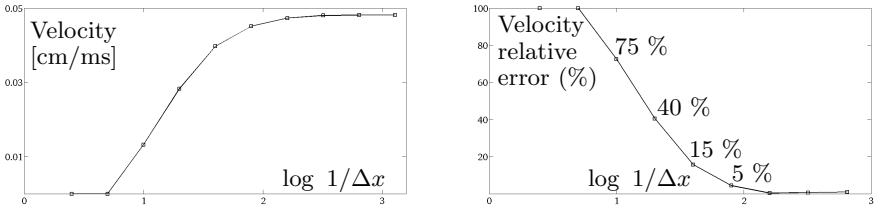

FIGURE 6. Relationship between the space resolution Δx and the pulses velocity. Left: pulse velocity as a function of $\log(1/\Delta x)$. Right: relative error between the pulse velocity and the limit (continuous model) velocity.

5.1. 1D case. — The domain Ω here is a 1D interval modelling a 40 cm long muscular fibre. Transmembrane potential waves (referred to as *pulses* here) propagating from the left towards the right of the domain are generated by applying a stimulation current at the left extremity of the fibre at initial time. For these simulations, the bidomain model has been set with the parameters in table 1 and $\chi = 2000$ cm^{-1}. The domain Ω is discretised with uniformly distributed grid points with a space resolution Δx varying from 4 mm up to 0.0075 mm. On figure 5, pulses corresponding to various space resolutions have been displayed at the same time $t = 50$ *ms* after stimulation. Strong discrepancies can be observed between the pulses velocities. These velocities have been computed and plotted as a function of the space resolution Δx in logarithmic

scale on figure 6 (left). As expected, the discrete pulses velocity converge towards a limit velocity as $\Delta x \to 0$. This limit velocity corresponds to the transmembrane potential wave velocity for the continuous model. The relative error between the (discrete) pulses velocity and this limit velocity has been plotted as a function of Δx (also in logarithmic scale) on figure 6 (right).

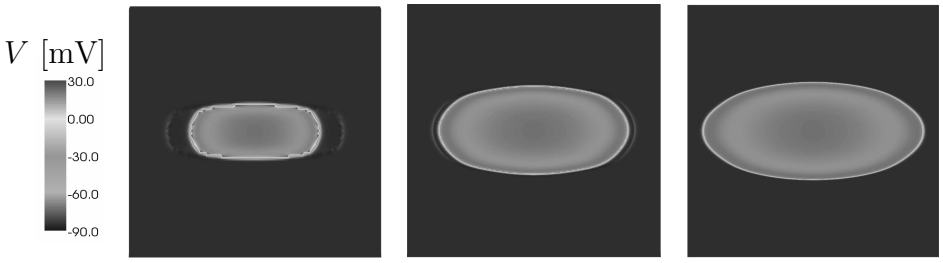

FIGURE 7. Space resolution influence on the transmembrane potential wavefront velocity and shape in dimension 2. The three transmembrane potential depicted here have been computed in the same way and recorded at the same time but on three different meshes with space resolutions of 0.23, 0.08 and 0.03 mm, from left to right respectively.

5.2. 2D case. — The former numerical results are investigated here in a more complex framework. The domain Ω is two dimensional (a 4×4 cm square). The bidomain system of equations has been discretised using the DDFV scheme presented in section 4 on unstructured triangular meshes. Fibre anisotropy is introduced with muscular fibres oriented horizontally.

The bidomain model has been set with the parameters from table 1. Different values of the scaling parameter χ are considered. Transmembrane potential waves are generated by applying a stimulation current at the domain centre.

On figure 7, three wavefront are displayed for the same value of $\chi = 2000$ cm^{-1} but on three meshes with different resolution (namely 0.23, 0.08 and 0.03 mm from left to right). The potential waves on the three meshes are represented at the sane time (37 ms after stimulation).
Potential waves have been computed for various values of χ (namely 250, 1000, 1500 and 2000 cm^{-1}) on a series of successively refined meshes with resolution varying from 0.25 to 0.03 mm. Their longitudinal and transverse velocities (along the horizontal and vertical axes) have been

computed. The continuous model corresponding velocities have been evaluated from a reference solution. The comparison between the computed velocities and the reference (limit) velocities is given in table 2. This table is designed to highlight what space resolution is needed to get a 1% accurate prediction on the wavefront velocities (axially and transversely to the fibre direction).

space resolution [mm]	0.16	0.12	0.08	0.06	0.04	0.03
$\chi = 250$ cm^{-1}	5.4 %	1.4 %				
$\chi = 1000$ cm^{-1}			17.3 %	2.9%		
$\chi = 1500$ cm^{-1}				14.0 %	1.6 %	
$\chi = 2000$ cm^{-1}				18.5 %	7.4 %	.6 %

TABLE 2. Relative error on the transmembrane potential wavefront velocities (axial and transverse), according to the scaling parameter χ and the space resolution.

5.3. Discussion. — The results in the one dimensional case display the general behaviour of the space-discretised bidomain equations. Transmembrane potential waves do exist at the continuous level. However, on a discrete lattice potential waves will not exist unless the space resolution of the lattice is finer than some critical value $\Delta x < \Delta x_0$. Whenever $\Delta x > \Delta x_0$, no waves can propagate: a well known *propagation failure* phenomenon occurs, see *e.g.* [**28**]. This is visible on figure 6 (left): the two first points on the left of the graph, with a space resolution of 4 and 2 mm, corresponding to a zero velocity are inside the propagation failure region. Although potential waves do propagate when $\Delta x < \Delta x_0$, these waves may be considerably slowered. This is illustrated on figure 5: the pulse on the left (1 mm space resolution) is four times slower than the limit pulse in bold dash line (reference solution). Thus, a very careful attention has to be paid with the choice of the space resolution when discretising the bidomain model. Actually, as depicted on figure 6 (right), the propagation failure region is followed by a range of space resolution producing considerable relative error on the velocities as compared to the reference solution. For instance, from a 1 to a 0.1 mm space resolution, the relative error on the velocity decreases from 75% to less than 5 % , a 0.05 mm resolution being necessary to get an accuracy of order 1%. Another interesting feature is illustrated on figure 6: the space resolution influence on the length of the pulses plateau. As already mentioned in the

preamble of this section, the space resolution has a negligible influence on the APD. Here APD corresponds to the ratio between the plateau length and the pulse velocity. All pulses having the same APD, the slow pulses have shorter plateau length.

In dimension 2, the situation is even sharper. The same slowering effect of the discretisation is illustrated on figure 7. It is moreover reinforced by a degradation of the potential wavefront general shape on coarse mesh. In fact, an elliptic shape is expected for the wavefront here: coarsening the space resolution damages this shape. Therefore, a sufficiently fine space resolution has to be imposed not only to have an accurate prediction on the potential waves velocity but also to prevent the wavefront from distortion.

Being given a set of conductivities for the model and a discretisation scheme, the choice of the space resolution is dictated by the scaling parameter χ since this parameter controls the wavefront thickness. The setting of the space resolution with regard to the value of χ is given in table 2. To get an accuracy of order 1% on the transmembrane potential waves for a physiological range of values of χ (1500-2000 cm^{-1}) imposes a space resolution below 0.04 mm. On a 2 dimensional slice of the heart (50 cm^2 approximately), this requires a computation with roughly 5×10^6 degrees of freedom. In dimension 3, for one whole human heart (about 50 cm^3), 2×10^9 degrees of freedom are necessary.

To carry on with the numerical simulations, the value of χ will be lowered to 250 cm$-$1 in the sequel of this paper. A space resolution of 0.1 mm will thus be required, making the computational costs affordable.

6. Simulations on segmented medical images

The goal now is to compare the solutions obtained from the bidomain and adapted monodomain models on a more complex and realistic configuration: anatomical geometry of the heart and torso including fibrous anisotropy and conductivity heterogeneities. We first detail the specific aspects of the test case. The transmembrane potential, the extra-cellular and extra-cardiac potentials, and the ECG computed from the body surface potential recordings are next presented for both models. A discussion of the results follows.

6.1. The test case. — According to the conclusions reached in section 5, bi-dimensional simulations are done and the value of the scaling parameter χ is set to 250 to obtain accurate comparisons while maintaining affordable computational costs. The other parameters in the bidomain and adapted monodomain models are set as described in section 3.3.

6.1.1. The mesh. — The heart and torso mesh has been generated from the segmented medical images as described in section 2 and depicted on Figure 2. The heart itself counts 485 000 nodes, whereas the torso has 115 000 nodes, resulting in a mesh with 600 000 nodes for the entire thorax slice. Four sub-domains have been identified: ventricles, lungs, ventricle cavities (filled in with blood) and the remaining tissues. This mesh has a 0.1 mm resolution in the myocardium, enough to get an accuracy of 1 % on the action potential propagation velocity according to Table 2.

6.1.2. Fibre orientation. — The fibre orientation is required to set the conductance tensors σ_e and σ_i. No physiological data being available on the fibre organisation of the medical images used here, we artificially built the fibre orientation using the following anatomical rules: the muscular fibres are rotating around the ventricles cavities and are tangent both on the epicardial and endocardial walls. Such a fibre architecture is easy to construct from the level set solution computed in the segmentation process (2). Few fibres are shown in Figure 8a.

6.1.3. Activation sites and initial condition. — Action potential propagation is initiated by applying a stimulation current at four stimulation sites located on the endocard of both ventricles and depicted on Figure 8b. Physiologically, activation in the ventricles is generated by the fast conduction tissue (Purkinje fibres) not included in our model. Purkinje fibres induce ventricular myocites depolarisation at their extremities, which phenomenon is modelled here by applying localised stimulation currents causing the same depolarisation. Location of the initiation sites has been determined from physiological data in Durrer *et al* [**24**]. In this paper, action potential propagation isochrons in human ventricles have been measured. One of these isochrons has been reproduced on Figure 8c. Initiation sites are visible on the left and right ventricular endocard (4 sites), with a delay of 5 ms for the right ventricle activation. The rest of the myocardium is set to rest potential (-86.2 mV), while the extra-cellular and extra-cardiac potentials are set to zero.

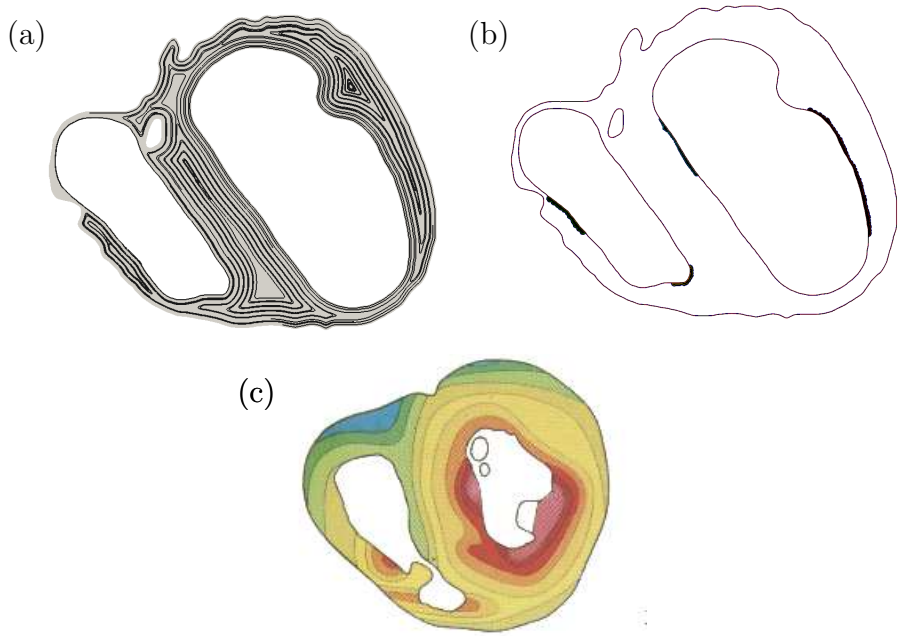

FIGURE 8. (a) Myocardial fibre organisation. (b) Stimulation sites. 4 stimulation zones are identified, two on the left ventricle endocard and two on the right one. The left ventricle is stimulated first, then the right ventricle with a delay of 5 ms. (c) Depolarisation wave isochrons from experimental measurements on perfused human ventricles (from Durrer *et al.* [**24**]), 5 ms separate the isolines.

6.1.4. Computing the ECG. — The extra-cardiac potential is recorded at the six points of the thorax labelled V1 to V6 shown on Figure 9. These six electrodes are located as closely as possible with a bi-dimensional geometry to their actual position on the chest in the standard ECG procedure. The electrode V1 is located slightly right to the sternum with the remaining electrodes aligned towards the left up to the armpit. Recordings are done at every time step, with the time step of 0.05 ms used in all our simulations. The raw values of the extra-cardiac potential are used to draw the ECG that will shown below.

6.2. Results. — The evolution of the solution of the bidomain model is depicted on Figure 10 at three consecutive times during the depolarisation phase. At the left, the transmembrane potential is shown. Depolarised regions (in red) spreads across the myocardium starting from

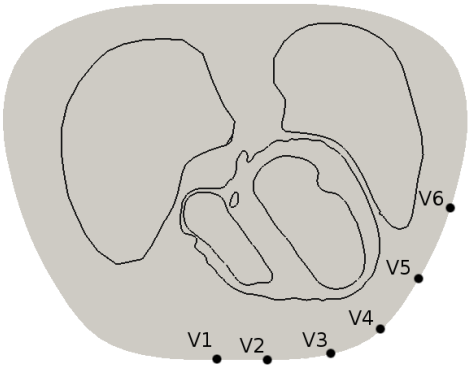

FIGURE 9. ECG recordings: position of the electrodes.

the initiation sites. The figures at the bottom shows the solution right after the depolarisation fronts coming from the right and left ventricle activation sites have crossed over in the septum.

Extra-cellular and extra-cardiac potential ϕ maps are depicted at the right on Figure 10. Different scales are used to plot the potentials V and ϕ as the potential ϕ has a smaller magnitude than the transmembrane potential V. In general, $V \in [-90, 35]$ mV while $\phi \in [-20, 20]$ mV. The fast positive inward ionic currents at the depolarisation front lead to a sharp increase of the transmembrane potential V (red regions on figures at the left) and a sudden decrease of the extra-cellular potential ϕ (blue regions on figures at the right). This is a simple consequence of the conservation of charges between the intra- and extra-cellular media expressed in the bidomain model. The fibre orientation is visible on the transmembrane potential V sequence, the depolarisation wavefronts propagating faster along the ventricle cavity boundaries–, tangent to the fibres–, than across the septum for instance. The depolarisation wavefront propagation leads to a strong polarisation of the extra-cellular medium ahead of the front (red regions on figures at the right). These myocardial areas with positive extra-cellular potential act as sources for the extra-cardiac potential, leading to a positive potential in the thorax and positive recordings at the electrodes on the chest.

6.2.1. Comparison of solutions from both models. — Solutions for the test case documented in the previous section are computed with both the bidomain and adapted monodomain models, using the same mesh, parameters and initial solution. Comparisons are made on the basis of

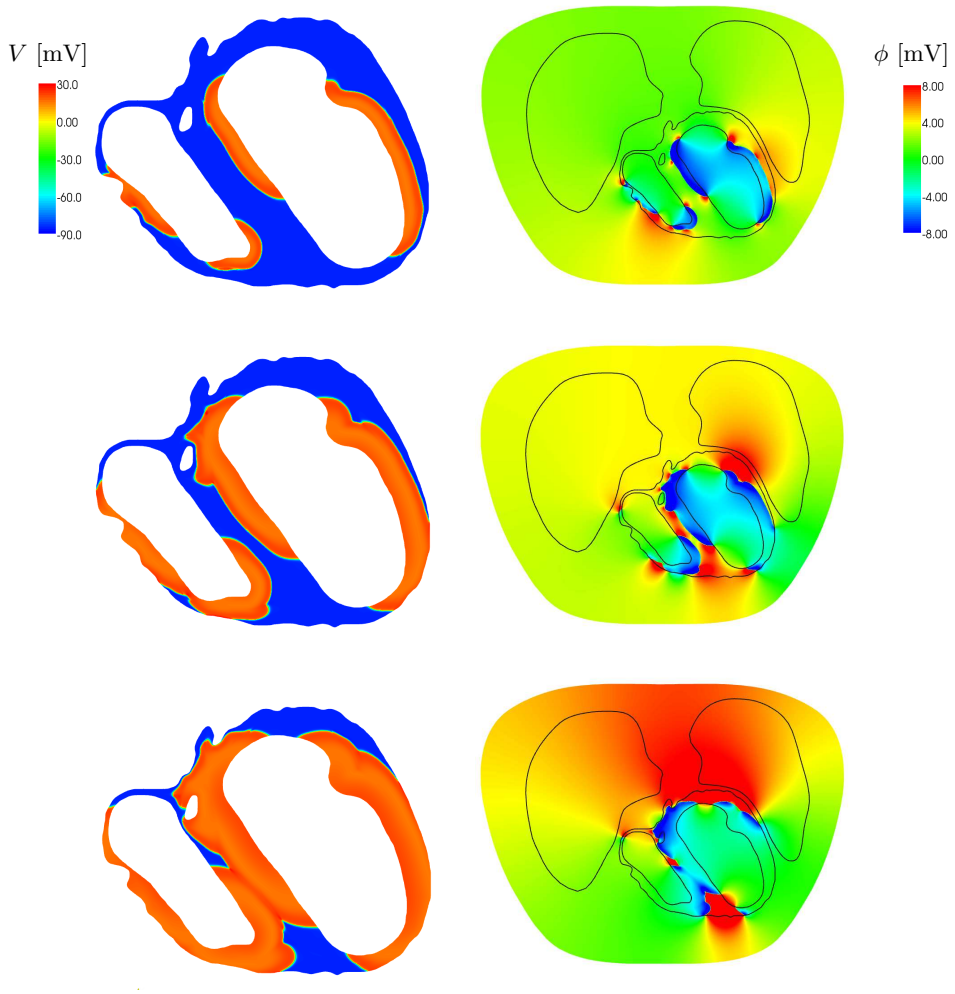

FIGURE 10. Left: from top to bottom, transmembrane potential V at times $t = 16$, 24 and 32 ms after initiation. Right: corresponding extra-cellular and extra-cardiac potential maps.

i) the de-/re-polarisation isochrons, ii) the potentials V and ϕ at given times and iii) the ECG recorded.

Figure 11 shows the depolarisation isochrons obtained with the two models. These isochrons are computed by checking at which nodes of the mesh that are in a non-activated polarised state the transmembrane

potential V increases above a threshold potential of 20 mV. This verification is done at each time step while solving any of the two models and the time at which each node depolarises is memorised. Initiation regions are seen in blue on both figures, while areas in red are last depolarised. The repolarisation isochrons are not shown here but closely match the depolarisation isochrons for both models. This situation is concordant with the setting of our model here for which no heterogeneities in the ionic model within the myocardium has been considered. Thus, the first cells to depolarise are the first to repolarise.

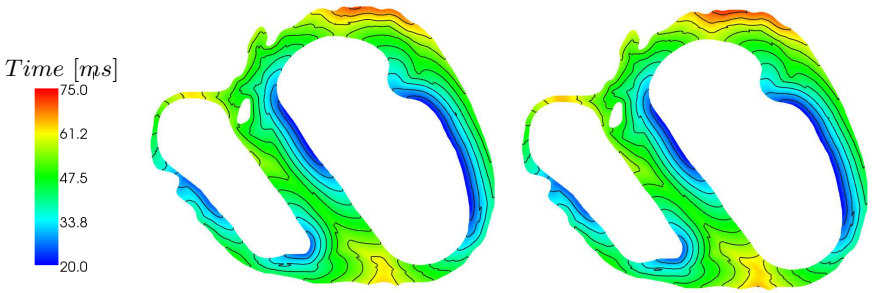

FIGURE 11. Depolarisation isochrons: bidomain model (left) and adapted monodomain model (right). The isochrons are separated by 5 ms.

Contours of V near the depolarisation front are superposed to the potential ϕ on Figure 12 (at the top) for both models. These V contours are drawn on the same figure (at bottom) to accurately compare the position of the depolarisation fronts predicted by the bidomain and adapted monodomain models. The solutions depicted correspond to the solution at time $t = 24$ ms seen on Figure 10 (middle), approximately corresponding to the mid-depolarisation sequence. Solutions at times $t = 16$ and 32 ms were also compared (not shown here). Similar trends were observed.

The ECG recorded at leads V1 and V5 are plotted on Figure 13 for both models. Similar graphs and trends were obtained at the other leads (not shown here). For each lead, a L^2 relative error is obtained by computing the absolute $L^2(0,T)$ error between the ECG for the adapted monodomain and bidomain models with $T = 600$ ms and by dividing this absolute error by the L^2 norm of the reference bidomain ECG. These relative errors for the six leads are reported in Table 3. Leads V1 and V5 have the smallest and largest L^2 relative error, respectively.

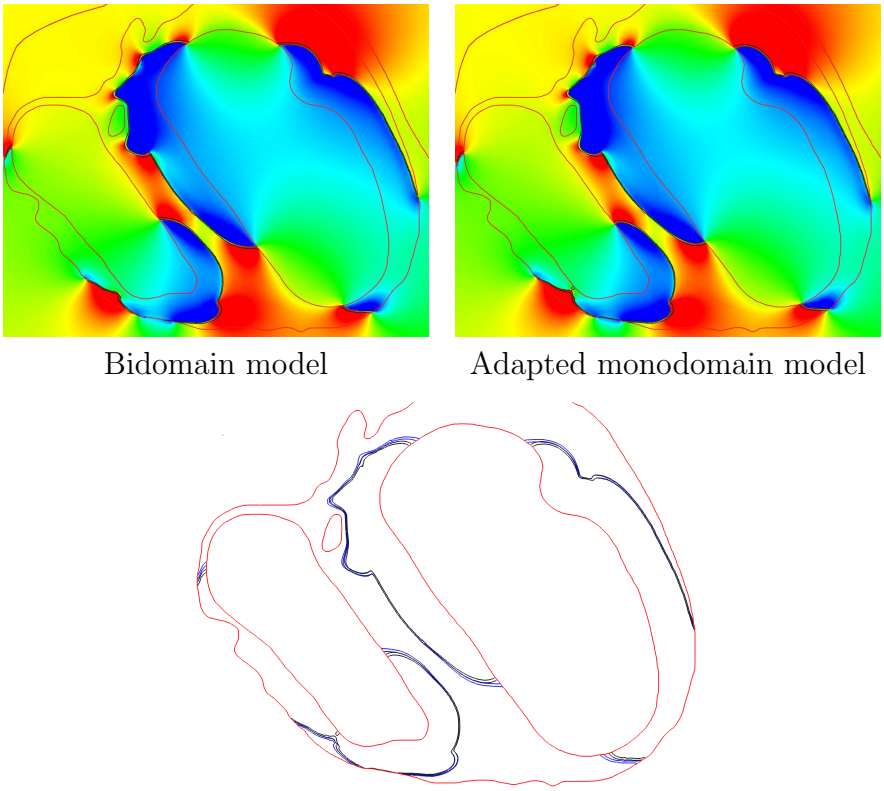

FIGURE 12. Comparison of the bidomain and adapted monodomain solutions at time $t = 24$ ms after initiation. Top: colours correspond to the extra-cellular and extra-cardiac potentials and contours to the transmembrane potential at $V =$ -80, -25, 30 mV. Bottom: superposition of these transmembrane potential contours for the bidomain (blue) and adapted monodomain (black) models.

lead	V1	V2	V3	V4	V5	V6
error	6.9	6.9	7.9	10.4	11.4	7.3

TABLE 3. Relative L^2 error (in %) between the bidomain and adapted monodomain ECG recordings at each lead.

6.2.2. Computational requirements for solving both models. — The computational requirements to solve the bidomain and adapted monodomain models are now compared. Computing the transmembrane potential V

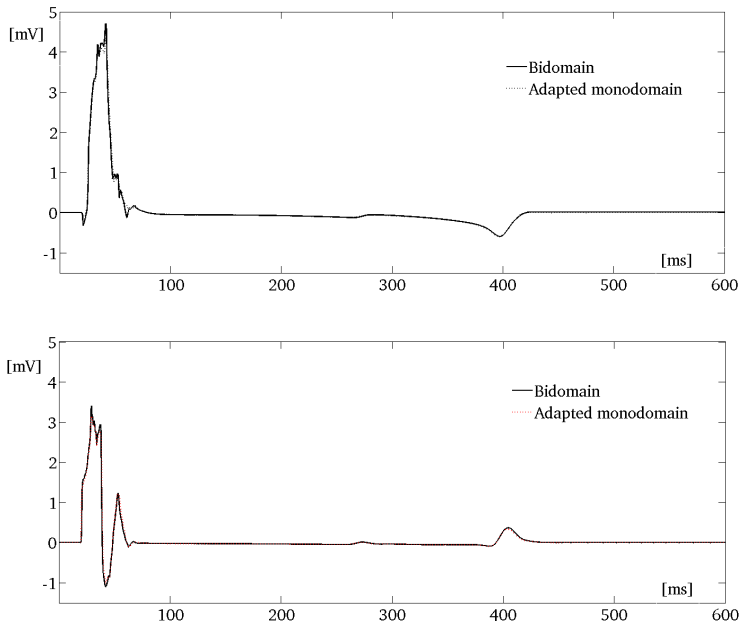

FIGURE 13. ECG at leads V1 and V5 for the bidomain and adapted monodomain models.

on the heart only takes about 1/50 of the total CPU time to solve the full bidomain model on the combined heart-thorax. We recall that the heart has 485 000 nodes while the heart-thorax counts 600 000 nodes. For this comparison, the same time-step $\Delta t = 0.05$ ms is used, the norm of the system residual must be below 10^{-8} and 10^{-7} for the adapted monodomain and bidomain models, respectively. Computing V and also the extra-cellular and extra-cardiac potential ϕ at each ms (every 20 time steps) during the simulations with the adapted monodomain model, the ratio of CPU times increases to 1/24. Solving the potential equation for ϕ is indeed difficult and the most CPU intensive. For the computation of ϕ with the adapted monodomain model, the norm of the system residual needed is 10^{-5} only.

The impact of the convergence tolerance on the residual of the bidomain model is now illustrated in Table 4 and Figure 14. The relative error on the ECG is taken between solutions at successive tolerances, e.g. between the ECG recorded at 10^{-5} and 10^{-4} tolerances with as reference solution the ECG at 10^{-5} tolerance. Computations were made on

coarser mesh to show that the relative error between ECG at successive tolerances closely matches the relative error between the ECG recorded at a given tolerance and a reference ECG at the strictest tolerance.

Tol	10^{-4}	10^{-5}	10^{-6}	10^{-7}
V1	68.1	65.9	30.4	8.3
V2	68.0	81.6	27.4	9.4
V3	72.8	90.9	28.2	10.2
V4	82.3	132.1	27.7	11.2
V5	84.5	60.7	38.7	14.5
V6	83.4	43.8	32.1	8.6

TABLE 4. Relative L^2 error (in %) between ECG recordings at each lead for bidomain solutions at successive tolerances.

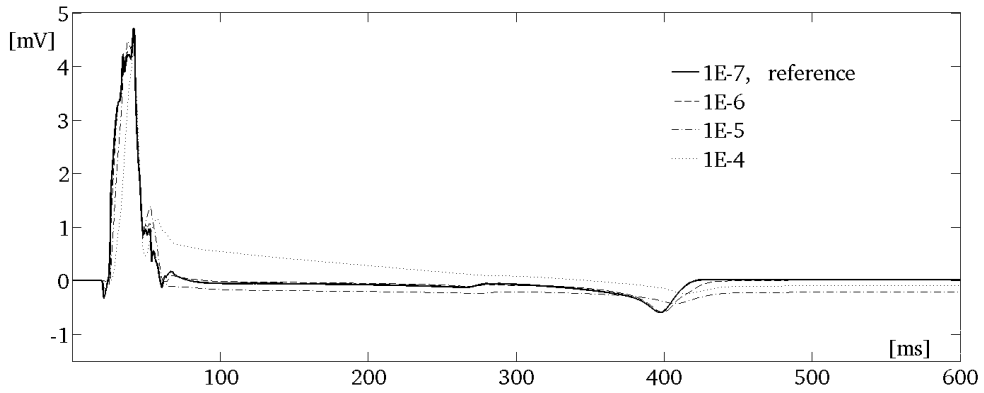

FIGURE 14. ECG recorded at electrod V1 using the bidomain model for various tolerances during the linear system inversion. ECGs depicted here correspond to a tolerance varying from 10^{-4} up to 10^{-7}. This last 10^{-7} tolerance corresponding to the reference solution of the bidomain model.

6.3. Discussion. — The isochrons of Figure 11 obtained with the bidomain and adapted monodomain models are relatively close to the experimental results of Durrer *et al.* [**24**] (see Figure 8 at bottom). The qualitative aspect of the isochrons is the same. The depolarisation time of the whole myocardium is of the same magnitude, i.e. about 50 ms from the initial activation to the last depolarisation times in both cases.

This is surprising as Durrer *et al.* used perfused human hearts in their experiments for which the fibre architecture and the action potential wave propagation are three-dimensional, while our simulations are two-dimensional. We have no clear explanation of this good agreement. A plausible cause is that the action potential propagates more within the cut plane than across the plane for this cross-section of the heart. Moreover, the membrane surface-to-volume ratio χ is equal to 250 cm^{-1} in our simulations while it is about 2000 cm^{-1} in myocardial tissue. The conductance velocity being proportional to $\chi^{-1/2}$ at least for one-dimensional waves and simple ionic models, the action potential generally propagates nearly 3 times slower with the physical value of χ than with $\chi = 250$ cm^{-1}. If it had been possible to use a larger χ, we might have seen larger discrepancies between the experimental and numerical results.

The results of the previous section show that the solutions of the bidomain and adapted monodomain models are very close to each other. This is seen by comparing the variables V and ϕ, the re-/de-polarisation isochrons and the ECG obtained with both models. The position of the depolarisation fronts closely match between models except for minor differences in a small area near the walls (see for instance Figure 12 at bottom). The fibres are taken tangent to the walls in our simulations, which implies that $\partial V/\partial n = 0$ for the transmembrane potential obtained through the adapted monodomain model. Within the accuracy limits imposed by the computational mesh, the contours of V are thus orthogonal to the heart walls. For the bidomain model, the boundary condition on V is given by $\partial V/\partial n = -\partial \phi_e/\partial n$ and the V contours are not orthogonal to the heart walls unless $\partial \phi_e/\partial n = 0$. This difference on the boundary conditions explains the slight contour mismatch near the walls for the two models. Away from the walls, the time evolution of V is controlled by transmembrane ionic currents which are the same in both models and by the conductance second order terms. For physiological values of the conductivity along and across fibres, using a single conductance operator with the harmonic average tensor σ_m in the partial-differential equation for V properly propagates the action potential wave. This is true at least in the case of "healthy" stimulation patterns and normal wave propagation used in our test case.

The isochrons of Figure 11 confirm this analysis, the in-time evolution of the depolarisation fronts are similar for both models. The fronts propagation for the adapted monodomain model appears as being slightly slower than with the bidomain model. The total amount of time needed for

the ventricles to entirely depolarise has been computed for both models, showing a difference of 3 % in relative error.

The ECG shown on Figure 13 are well superposed except for minor mismatches in zones with large gradients. A very tiny difference of time amplitude of the QRS complex can be seen, illustrating that the depolarisation is slightly slower with the adapted monodomain model than with the bidomain one. In comparison, the relative errors between the ECG obtained with the bidomain and adapted monodomain models given in Table 3 seem large for such a good match of the curves. This relative error is obtained by dividing the absolute error by the L^2 norm of the reference bidomain ECG. The ECG recordings being null for most times, this division scales up the relative error, explaining the large relative errors at leads V1 to V6 in spite of the excellent curve superposition.

While the solutions from the bidomain and adapted monodomain models show excellent agreement, the computational requirements to solve the two models are not the same. The bidomain model is by two orders of magnitude more demanding in CPU time if only the transmembrane potential V is required. The numerical solution of the coupled potential equations for the extra-cellular potential ϕ_e and extra-cardiac potential ϕ_T is the most intensive. The stiffness of these potential equations is the main cause of error on the ECG recovered from the bidomain model when the norm of the residual is not reduced enough by the iterative method, as presented in Table 4 and Figure 14. The minimal requirement for getting an accurate ECG is to solve the potential equations with a tolerance of at most 10^{-7} on the residual. This tolerance is harder to achieve with the bidomain model where the coupling of the potential equations with the reaction-diffusion equation for V makes the design of good preconditioner more difficult.

If the extra-cellular and extra-cardiac potentials were recovered at each time step for the adapted monodomain model, the computational saving in using the monodomain model would be much smaller. Indeed, these potential equations are uncoupled from the reaction-diffusion equation for V in the adapted monodomain model, leaving the possibility of computing the potential ϕ every n time steps only. In Figure 13, ECG recordings every 20 time steps for the monodomain model allow for a great saving in CPU time and are as accurate as those for the bidomain models done at every time step.

7. Conclusion

The action potential and ECG computed with a bidomain and an adapted monodomain models were compared using a two-dimensional test case. The geometry used is derived from a patient-based CT scan and represents a two-dimensional cut of the heart embedded in a torso. By segmenting the CT image with an automatic level-set method and meshing this level-set geometry with an appropriate mesh generator, we easily did electrophysiological simulations on a patient-based geometry. The results show that monodomain models can predict reliable cardiac action potential and ECG when the activation sites reside within the myocardium, this at a much lower cost than with the bidomain model. Here "reliable" means that the results are as good as those from the bidomain model which is generally considered the best model for coupled heart-thorax simulations. The comparison of the computed ECG with real patient ECG is another issue, strongly dependent on the ionic models representing the myocite channel activity. Our conclusions simply say that given the best ionic models, a properly set monodomain model will provide as realistic ECG as the bidomain model, and if the bidomain model does not match reality then a monodomain model will not do it either, and vice-versa.

Our conclusions still need to be confirmed on patient-based three-dimensional geometries and with a physiological value of the surface-to-volume ratio χ. The techniques behind the pipeline from medical images to electrophysiological simulations can easily be extended to three dimensions. Developments are well under way and will be reported in a forthcoming paper. Moreover we played enough with χ in previous simulations to be confident that a higher χ should not change the conclusions. As shown with our computations, a physiological χ needs very fine meshes, beyond what is possible in three dimensions with uniformly fine grids. The use of local mesh refinement as in [**11**] or of anisotropic mesh adaptation as in [**3**] is a promising avenue for reaching physiological χ and compare models on three-dimensional heart geometries. Another outstanding issue is the identification of situations where both models give discordant solutions and ECG, away from the cases of common activation sites and normal heartbeat used here, and the verification with computations that indeed the bidomain and monodomain predictions are quantitatively and qualitatively different for these pathological situations.

Acknowledgements

The authors would like to thank the *Centre de Recherches Mathématiques* (CRM) of the *Université de Montréal* for providing a post-doctoral fellowships to the first author, and the *Laboratoire de Mathématiques et de leurs Applications de Pau* of the *Université de Pau et des Pays de l'Adour* (UPPA) for covering travelling expenses of the first and third authors. This work was also supported by a NSERC Discovery Grant and a NSERC post-graduate scholarships to the second author. Special thanks to the *University of Ottawa Heart Institute* for providing the CT scan data that were used for building our heart model.

References

[1] L. Ambrosio, N. Fusco, and D. Pallara. Functions of bounded variation and free discontinuity problems. *Oxford Mathematical Monographs*, 2000.

[2] Luigi Ambrosio, Piero Colli Franzone, and Giuseppe Savaré. On the asymptotic behaviour of anisotropic energies arising in the cardiac bidomain model. *Interfaces Free Bound.*, 2(3):213–266, 2000.

[3] Y. Belhamadia, A. Fortin, and Y. Bourgault. An accurate numerical method for monodomain models using a realistic heart geometry. *Mathematical Biosciences*, submitted, 2008.

[4] O. Berenfeld and J. Jalife. Purkinje-muscle reentry as a mechanism of polymorphic ventricular arrhythmias in a 3-dimensional model of the ventricles. *Circ. Res.*, 82:1063–1077, 1998.

[5] Y. Bourgault, Y. Coudière, and C. Pierre. Existence and uniqueness of the solution for the bidomain model used in cardiac electrophysiology. *Nonlinear Analysis: Real World Applications*, 10(1):458–482, 2009.

[6] ML. Buist and AJ. Pullan. Torso coupling techniques for the forward problem of electrocardiography. *Annals Biomed. Eng.*, 30(10):1299–1312, 2002.

[7] ML. Buist and AJ. Pullan. The effect of torso impedance on epicardial and body surface potentials: a modeling study. *IEEE Trans. Biomed. Eng.*, 50(7):816–824, 2003.

[8] T.F. Chan and L.A. Vese. Active contours without edges. *Image Processing, IEEE Transactions on*, 10(2):266–277, 2001.

[9] JC. Clements, J. Nenonen, P K. Li, and M. Horácek. Activation dynamics in anisotropic cardiac tissue via decoupling. *Annals Biomed. Eng.*, 32(7):984–990, 2004.

[10] L. Clerc. Directional differences of impulse spread in trabecular muscle from mammalian heart. *J. Physio.*, 255(2):335–346, 1976.

[11] P. Colli Franzone, P. Deuflhard, B. Erdmann, J. Lang, and L. F. Pavarino. Adaptivity in space and time for reaction-diffusion systems in electrocardiology. *SIAM J. Sci. Comput.*, 28(3):942–962 (electronic), 2006.

[12] P. Colli Franzone and L. Guerri. Spreading of excitation in 3-D models of the anisotropic cardiac tissue. I. Validation of the eikonal model. *Math. Biosci.*, 113:145–209, 1993.

[13] P. Colli Franzone, L. Guerri, and E. Magenes. Oblique double layer potentials for the direct and inverse problems of electrocardiology. *Math. Biosci.*, 68(1):23–55, 1984.

[14] P. Colli Franzone, L. Guerri, M. Pennacchio, and B. Taccardi. Spread of excitation in 3-D models of the anisotropic cardiac tissue. II. Effects of fiber architecture and ventricular geometry. *Math. Biosci.*, 147(2):131–171, 1998.

[15] P. Colli Franzone, L. Guerri, and S. Rovida. Wavefront propagation in an activation model of the anisotropic cardiac tissue: Asymptotic analysis and numerical simulations. *J. Math. Biol.*, 28(2):121–176, 1990.

[16] P. Colli Franzone, L. Guerri, and S. Tentoni. Mathematical modeling of the excitation process in myocardial tissue: Influence of fiber rotation on wavefront propagation and potential field. *Math. Biosci.*, 101(2):155–235, 1990.

[17] P. Colli Franzone, L. Guerri, and C. Viganotti. Oblique dipole layer potentials applied to electrocardiology. *J. Math. Biol.*, 17(1):93–124, 1983.

[18] P. Colli-Franzone, L. Guerri, C. Viganotti, E. Macchi, S. Baruffi, S. Spaggiari, and B. Taccardi. Potential fields generated by oblique dipole layers modeling excitation wavefronts in the anisotropic myocardium. *Circ. Res.*, 51:330–346, 1982.

[19] P. Colli-Franzone, LF. Pavarino, and B. Taccardi. Simulating patterns of excitation, repolarization and action potential duration with cardiac Bidomain and Monodomain models. *Math. Biosci.*, 197(1):35–66, 2005.

[20] P. Colli-Franzone and G. Savaré. Degenerate evolution systems modeling the cardiac electric field at micro- and macroscopic level. *Evolution equations, semigroups and functional analysis*, 2002.

[21] Y. Coudière and C. Pierre. Stability and convergence of a finite volume method for two systems of reaction-diffusion equations in electrocardiology. *Nonlinear Analysis: Real World Applications*, 7(4):916–935, 2006.

[22] Y. Coudiere, C. Pierre, O. Rousseau, and R. Turpault. 2D/3D DDFV scheme for anisotropic- heterogeneous elliptic equations, application to electrograms simulation from medical data. *Int. J. Finite Volumes*, 2009.

[23] Komla Domelevo and Pascal Omnès. A finite volume method for the Laplace operator on almost arbitrary two-dimensional grids. *M2AN*, 39(6):1203–1249, 2005.

[24] D. Durrer, RT. Van Dam, GE. Freud, Janse MJ., Meijler FL., and ArzBaecher RC. Total excitation of the isolated human heart. *Circulation*, 41:899–912, 1970.

[25] M. Ethier and Y. Bourgault. Semi-implicit time discretization schemes for the bidomain model. *SIAM Journal of Numerical Analysis*, 46(5):2443–2468, 2008.

[26] F. Hermeline. A finite volume method for the approximation of diffusion operators on distorted meshes. *J. Comput. Phys.*, 160(2):481–499, 2000.

[27] AL. Hodgkin and AF. Huxley. A quantitative description of membrane current and its application to conduction and excitation in nerve. *J. Physiol.*, 117:500–544, 1952.

[28] J. P. Keener. Propagation and its failure in coupled systems of discrete excitable cells. *SIAM J. Appl. Math.*, 47:556–572, 1987.

[29] W. Krassowska and JC. Neu. Homogenization of syncytial tissues. *CRC Crit. Rev. Biomed. Eng.*, 21(2):137–199, 1993.

[30] W. Krassowska and JC. Neu. Effective boundary conditions for syncytial tissues. *IEEE*, 41(2):143–150, 1994.

[31] P. Le Guyader, F. Trelles, and P. Savard. Extracellular measurement of anisotropic bidomain myocardial conductivities. I. theoretical analysis. *Annals Biomed. Eng.*, 29(10):862–877, 2001.

[32] GT. Lines, P. Grottum, AJ. Pullan, J. Sundes, and A. Tveito. Mathematical models and numerical methods for the forward problem in cardiac electrophysiology. *Comput. Visual. Sci*, 5:215–239, 2002.

[33] GT. Lines, P. Grottum, and A. Tveito. Modeling the electrical activity of the heart: a bidomain model of the ventricles embedded in a torso. *Comput. Viual. Sci.*, 5:195–213, 2003.

[34] Leon LJ. and M. Horácek. Computer model of excitation and recovery in the anisotropic myocardium. ii. excitation in the simplified left ventricle. *J Electrocardiol.*, 24(1):17–31, 1991.

[35] CH. Luo and Y. Rudy. A Dynamic Model of the Cardiac Ventricular Action Potential I. Simulations of Ionic Currents and Concentration Changes. *Circ. Res.*, 74:1071–1096, 1994.

[36] RS. MacLeod, B. Taccardi, and RL. Lux. The influence of torso inhomogeneities on epicardial potentials. *Computer in Cardiology*, pages 793–796, 1994.

[37] D. Mumford and J. Shah. Optimal approximations by piecewise smooth functions and associated variational problems. *Comm. Pure Appl. Math.*, 42(5):577–685, 1989.

[38] AV. Panfilov and JP. Keener. Re-entry in three-dimensional Fitzhugh-Nagumo medium with rotational anisotropy. *Physica D*, 84(3-4):542–552, 1995.

[39] PO. Persson and G. Strang. A Simple Mesh Generator in MATLAB. *SIAM Review*, 46(2):329–345, 2004.

[40] C. Pierre. Modelling and simulating the electrical activity of the heart embedded in the torso, numerical analysis and finite volumes methods. . *PhD Thesis, Université de Nantes*, 2005.

[41] M. Potse, B. Dube, J. Richer, A. Vinet, and RM. Gulrajani. A comparison of monodomain and bidomain reaction-diffusion models for action potential propagation in the human heart. *IEEE Trans. Biomed. Eng.*, 53(12):2425–2435, 2006.

[42] BJ. Roth. Action potential propagation in a thick strand of cardiac nuscle. *Circ. Res.*, 68:162–173, 1991.

[43] K. Simelius, J. Nenonen, and M. Horácek. Modeling cardiac ventricular activation. *Int. J. Bioelectromag.*, 3(2):51–58, 2001.

[44] NP. Smith, ML. Buist, and AJ. Pullan. Altered t wave dynamics in contracting cardiac model. *J. Cardiovascular Electrophysio.*, 14:5203–5209, 2003.

[45] MS. Spach, JF. Heidlage, PC. Dolber, and RC. Barr. Extracellular Discontinuities in Cardiac Muscle Evidence for Capillary Effects on the Action Potential Foot . *Circ. Res.*, 83:1144–1164, 1998.

[46] MS. Spach and Dolber PC. Relating extracellular potentials and their derivatives to anisotropic propagation at a microscopic level in human cardiac muscle. Evidence for electrical uncoupling of side-to-side fiber connections with increasing age. *Circ. Res.*, 58:356–371, 1986.

[47] KH. Ten Tusscher, D. Noble, PJ. Noble, and AV. Panfilov. A Model for Human Ventricular Tissue. *Am J Physiol Heart Circ Physiol*, 286, 2004.

[48] A. Tsai, A. Yezzi Jr, and A.S. Willsky. Curve evolution implementation of the Mumford-Shah functional for image segmentation, denoising, interpolation and magnification. *IEEE Trans. Image Processing*, 10(8):1169–1186, 2001.

[49] L. Tung. A bidomain model for describing ischemic myocardial D-D properties. *Ph.D. thesis, M.I.T.*., 1978.

[50] M. Veneroni. Reaction-diffusion systems for the microscopic cellular model of the cardiac electric field. *Math. Methods Appl. Sci.*, 29(14):1631–1661, 2006.

Charles Pierre, Laboratoire de Mathématiques et de leurs Applications de Pau, CNRS, Université de Pau et des Pays de l'Adour.
E-mail : charles.pierre@univ-pau.fr

Olivier Rousseau, Department of mathematic and statistics, University of Ottawa.
E-mail : orous097@uottawa.ca

Yves Bourgault, Department of mathematic and statistics, University of Ottawa.
E-mail : ybourg@uottawa.ca